Intermetallics 17 (2009) 445–452

Contents lists available at ScienceDirect

Intermetallics

journal homepage: www.elsevier.com/locate/intermet

Deformation and fracture behaviors of Co-based metallic glass and its composite with dendrites

J.T. Fan [a,b,*], Z.F. Zhang [a,*], S.X. Mao [c], B.L. Shen [d], A. Inoue [e]

[a] Shenyang National Laboratory for Materials Science, Institute of Metal Research, Chinese Academy of Science, 72 Wenhua Road, Shenyang 110016, PR China
[b] Department of Mechanical Engineering, The Hong Kong Polytechnic University, Hong Kong, PR China
[c] Department of Mechanical Engineering, University of Pittsburgh, Pittsburgh, PA 15261, USA
[d] Ningbo Institute of Materials Technology and Engineering, Chinese Academy of Sciences, Ningbo, 315201, PR China
[e] Institute for Materials Research, Tohoku University, Sendai 980-8577, Japan

ARTICLE INFO

Article history:
Received 30 September 2008
Received in revised form
21 November 2008
Accepted 10 December 2008
Available online 15 January 2009

Keywords:
B. Glasses, metallic
A. Composite,based on the metallic glass matrix intermetallics, miscellaneous
B. Deformation map
B. Fracture toughness
B. Mechanical properties at ambient temperature

ABSTRACT

Microstructures and mechanical properties of Co-based metallic glass with nominal composition of $Co_{43}Fe_{20}Ta_{5.5}B_{31.5}$ (at.%) cast at the different cooling rates were investigated. When cooling rate is low enough, some dendritic crystalline phases were in situ precipitated from the glass matrix, forming the Co-based metallic glass composite with dendrites. Macroscopically, the fully amorphous samples often split apart or were broken into some particles, displaying a fragmentation failure mode. The size of particles became larger with the decrease in cooling rate. But, strength reduces slightly. Besides, the composites with dendrites show a small compressive plasticity, plus local melting behaviors with vein-like structure on the fracture surfaces. Furthermore, the effects of cooling rate on microstructures, deformation and fracture behaviors were discussed systemically. It is proposed that the fragmentation mechanism can be attributed to the inherent brittle character and high stress concentrations around the free volume. And the local melting behavior is due to the more receiving elastic energy and local shearing.

1. Introduction

The rapid scientific and technological progresses constantly require the development of the novel materials with unique physical, chemical and mechanical properties. Therefore, many scholars have been devoting to the finding of new alloy with high performance for the need of times. With the birth of metallic glass as a novel class of metallic alloy in 1960, the history of materials science opened a new chapter [1]. Especially, the development of bulk metallic glass (BMG) alloy has attracted tremendous industrial attention and scientific interest, due to the high strength [2,3], which offers a great potential for structural application. At the same time, they also offer a new opportunity to reveal scientifically the fundamental deformation and fracture mechanisms of materials with super-high strength [4–10]. Especially, the strength reached the historical zenith about 5300 MPa under compression test for the amorphous Co–Fe–Ta–B alloy. However, it always displays a zero-plasticity fracture with a fragmentation failure mode [11]. Generally, the apparent macroscopic brittleness severely impedes further development of Co-based BMG materials, even though the strength is the highest among the BMG family. Therefore, it is significantly important to study its deformation and fracture behaviors, in order to explore the methods to improve the plasticity.

It is well known that at high stress and low temperature far below the glass transition point, BMGs usually exhibit inhomogeneous deformation, which is highly localized into the narrow shear bands, followed by the rapid propagation of shear bands across the sample, and subsequently premature catastrophic fracture [3,12]. These characters bring out an urgent question: why do the BMGs always display poor plasticity and how to improve it [13–15]. Recently, it is found that the mechanical properties of some Zr-based BMGs with the same composition are relatively sensitive to the cooling rate [16]. Besides, Huang et al. [17] have found a dramatic effect of sample size on the plastic deformation capability of a Ti-based BMG, suggesting a tendency, i.e., "smaller is

* Corresponding authors. Shenyang National Laboratory for Materials Science, Institute of Metal Research, Chinese Academy of Science, 72 Wenhua Road, Shenyang 110016, PR China.
E-mail addresses: mmjtfan@polyu.edu.hk (J.T. Fan), zhfzhang@imr.ac.cn (Z.F. Zhang).

0966-9795/$ – see front matter © 2008 Elsevier Ltd. All rights reserved.
doi:10.1016/j.intermet.2008.12.004

softer". And Hays et al. [14] reported the enhanced plastic strain, impact resistance and toughness of Zr-based BMGs with the ductile dendrites, prepared by controlling cooling rate. Thus, whether Co-based BMGs can also exhibit the improved mechanical properties, correlative to the cooling rate or not?

In this work, we successfully cast the $Co_{43}Fe_{20}Ta_{5.5}B_{31.5}$ alloy under the different cooling rates until the precipitation of dendritic crystalline phases. They all display brittle fragmentation fracture. But the fragmentation coefficient, F_n, [11] is much different, exhibiting a decreasing tendency with the decrease in cooling rate. When the sample was cast at the enough low cooling rate, Co-based BMGs composite could be formed with the in situ precipitated dendritic crystalline phases, which displayed a small plasticity of about 0.3% under the uniaxial compressive load.

2. Experiments

Multi-component Co-based alloy ingots with a nominal composition of $Co_{43}Fe_{20}Ta_{5.5}B_{31.5}$ (at.%) were prepared by arc melting the mixtures of ultrasonically cleansed Co, Fe, Ta metals with the purity of 99.99% or better and pure crystalline B (99.5 mass%) in a Ti-gettered highly pure argon atmosphere. Alloy ingots in a rod form with 2 mm in diameter were prepared by an ejection copper mold casting method. Each ingot was re-melted at least four times, in order to ensure the chemical homogeneity. At the same time, the time of arc melting was controlled into 3, 6 and 9 min, which led to the different initial temperatures of melting liquid and further contributed to the different cooling rates. Thus, three groups of samples were cast and designated as samples A, B, and C in terms of the cooling rate from high to low.

And then, all the samples were machined and polished into cylindrical bars with the same dimension of $\phi 2 \times 4$ mm for compressive test. In addition, one typical sample from each group was etched with hydrofluoric acid so as to expose the microstructure, and then examined by Quanta 600 scanning electron microscope (SEM). Meanwhile, all the as-cast samples were analyzed by X-ray diffraction (XRD) using a Rigaku diffractometer with Cu-K_α radiation as a source. The glass transition temperature and crystallization temperature were determined by Perkin–Elmer differential scanning calorimeter (DSC-7) under the flowing purified argon gas at a heating rate of 1 K/s. At last, the compressive tests were performed on a computed-controlled, servo-hydraulic Instron-8810 testing machine at a strain rate of $1 \times 10^{-4}\ s^{-1}$ at room temperature. For each group, three specimens or more were tested, and the averaged data were used. The deformation and fracture morphologies were observed by using Quanta-600 SEM.

3. Experimental results

3.1. Microstructures and thermal analyses

Fig. 1 shows the corresponding XRD patterns recorded from the cross-section of the as-cast alloy of samples A, B, and C. The patterns of samples A and B consist of only a series of broad diffraction maxima without any detectable sharp Bragg peaks. This indicates that the microstructure is fully amorphous glass. Meanwhile, the observations from the etched side surfaces of samples A and B give no hint for any visible crystallization phase [Fig. 2(a)]. Therefore, it can be concluded that samples A and B should have a fully amorphous structure, which is consistent with the previous results [9].

However, with decrease in cooling rate during solidification, some crystalline phases began to precipitate from the glassy matrix. It can be seen that the XRD pattern of sample C is composed of a broad diffusion background and a set of several sharp

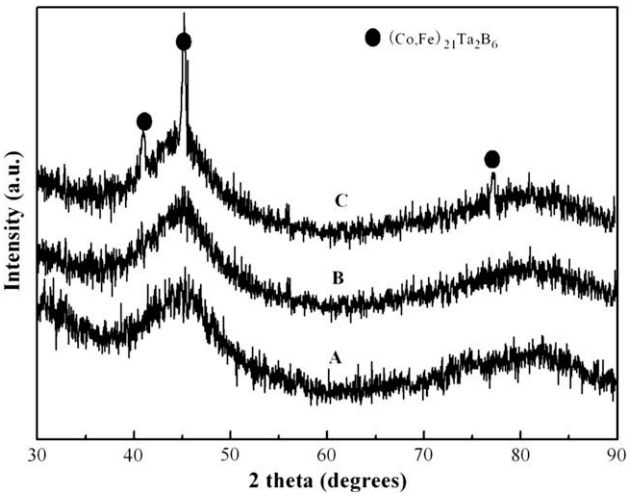

Fig. 1. XRD diffraction patterns taken from the cross-section surfaces of samples A, B and C with different cooling rates.

crystalline peaks, corresponding to a mixture of the glassy matrix and the precipitated crystalline phase, as shown in Fig. 1. The precipited phase was identified as a complex face-centered cubic $(Co,Fe)_{21}Ta_2B_6$ phase, similar to the previous report [18]. Besides, no other crystalline phases can be detected within the sensitivity limit of the XRD. Fig. 2(b) shows the SEM backscattered micrograph of the as-cast alloys on the etched cross-sectional surface. It is interesting to find that the bright phases, corresponding to the dendrites, disperse in the glassy matrix homogeneously. The dendritic structure is the character with primary dendrite axes with a length range of 10–20 μm. Besides, a regular pattern of secondary dendrite arms is several micron and even nanoscale space of 50–5000 nm. There is no any trace of the thick reaction layer at the interface between precipitated crystalline phase and glassy matrix. And neither pores nor voids appear over the whole cross-section of the samples. So, it is apparent that sample C should be the glassy composite with some in situ precipitated dendritic crystalline phases.

Fig. 3 displays the DSC profiles of samples A, B and C. All the samples exhibit one endothermic event, characteristics of the glass transition to a supercooled liquid state, followed by a distinct glass transition and undercooled liquid region, and then a very weak second exothermic reaction associated with crystallization of the supercooled liquid. However, the glass transition temperature, T_g, the first crystallization temperature, T_{x1} and the extent of undercooled liquid region, ΔT_x (defined by $(T_x - T_g)$), are slightly different. For sample A, they are 905 K, 976 K and 71 K, very similar to the previous report [9]. For sample B, they are 917 K, 977 K and 60 K. And for sample C they are 929 K, 984 K and 55 K, respectively. Besides, the weak second crystallization temperature, T_{x2}, was 1175, 1179, and 1176 K, respectively for samples A, B and C. All the data are listed in Table 1. Besides, the change in enthalpy, ΔH_0, is clearly different from the DSC pattern (inset in Fig. 3). The value, ΔH_0, associating with the exothermic peak, was calculated by integrating the heat flow near the glass transition range (600–920 K). The results are 4.2, 3.9 and 2.4 J/g for samples A, B, and C respectively, as listed in Table 1. Furthermore, the sum of the crystallization enthalpy $\sum \Delta H$ is equal to the sum of the exothermic heats for the first and the second crystallizations, that is,

$$\sum \Delta H = \Delta H_1 + \Delta H_2 \quad (1)$$

By calculating the exothermic heats of the first and second crystallizations, i.e., ΔH_1 and ΔH_2, it is also found that the sum of the

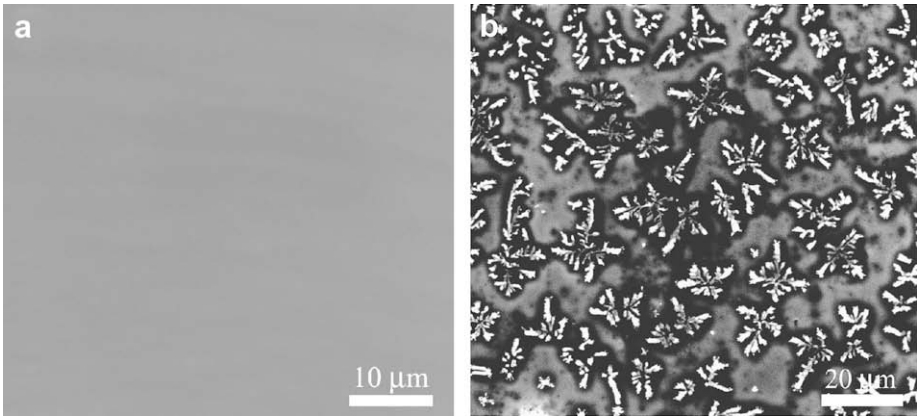

Fig. 2. SEM backscattered electron micrograph of the etched surface: (a) the typical featureless image of samples A and B; (b) the in situ precipitated dendritic crystalline phases.

crystallization enthalpy, $\sum \Delta H$, decreases from 44.7 to 43.3 J/g for the samples A and B with the fully amorphous structure. For the composite sample C, the value $\sum \Delta H$ declines down to 38.4 J/g. The above results indicate that the samples A, B, and C should have a different microstructures in detail. On the other hand, based on the DSC data during crystallization, for sample C, it is possible to calculate the volume fraction of the in situ precipitated crystalline phases from the difference in enthalpy. So, the volume fraction of crystalline phases was calculated to be about 12%, using the method reported in Ref. [19].

To sum up, for the current $Co_{43}Fe_{20}Ta_{5.5}B_{31.5}$ alloy, the variation in cooling rate led to the change in the microstructure, and even contributed to the precipitation of the dendritic crystalline phases, as represented by the difference in the XRD pattern and the exothermic reactions during DSC.

3.2. Mechanical properties

Fig. 4 presents the compressive stress–strain curves tested at room temperature for the current glassy alloy with the different cooling rates. The compressive properties of samples A, B and C, including Young's modulus, yield strength, fracture strength, elastic strain, and plastic strain, are listed in Table 2. For samples A and B, the stress–strain relation is linear up to the elastic strain of about 2.4%, but no distinct plastic deformation was observed. The Young's modulus, E, is very high, about 214 and 194 GPa for samples A and B. At the same time, the fracture strength of sample B, about 4700 MPa, is slightly lower than that (~5100 MPa) of sample A, which should be relative to the difference in their microstructures.

Furthermore, for sample C, its stress–strain relation is linear up to an elastic strain of about 2.6%, followed by yielding and then a slight plastic deformation, about 0.3%. This implies that the plasticity is significantly different from that of samples A and B. Besides, its yield strength is approximately equal to its fracture strength, about 4400 GPa. Evidently, the strength of sample C is lower than that of samples A and B. Meanwhile, the Young's modulus, E is about 175 GPa, also smaller than that of samples A and B. Those results illuminate that low cooling rate might vary the microstructure of metallic glass alloys, and improves the plasticity via in situ precipitating dendritic crystalline phases.

To sum up, with the decrease in cooling rate, the plasticity prior to failure is improved, but the Young's modulus, E and strength decrease, suggesting a soft trend. This indicates that cooling rate plays a crucial role in the ability of resisting deformation and the plasticity of metallic glass materials.

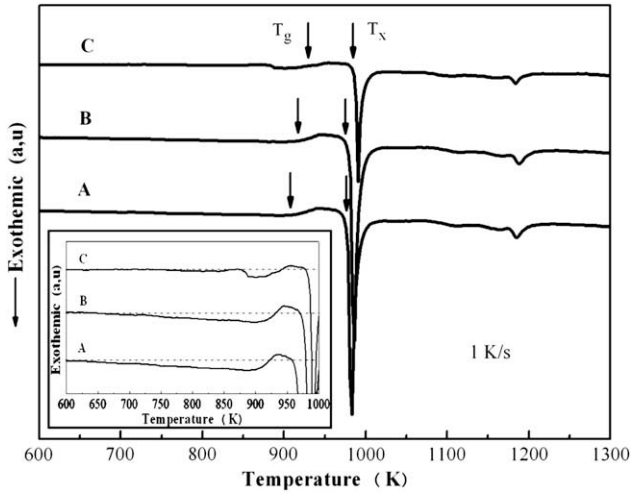

Fig. 3. DSC traces of samples A, B and C, at a heating rate of 1 K/s, and the inset clearly shows the different in the enthalpy, ΔH_0.

3.3. Fracture morphologies

Fig. 5 shows the SEM images of the fractured particles with different sizes after subjected to the uniaxial compressive test. During compressive test, all the samples emitted a shrill sound like bomb blasting without any premonition. If the compressive experiment process was recorded by a camera, there is no any visible light emission during fracture, not similar to the compressive fracture moment of Zr-based BMGs [20]. At last, all the samples broke into many fine particles or even powders, exhibiting a fragmentation failure mode [11], as depicted in Fig. 5(a) and (c). However, it is interesting to find that the size of the particles is significantly different. That is about 100–400 μm (sample A), 400–1000 μm (sample B), and 1–2 mm or larger (sample C), suggesting an increasing tendency with the decrease in cooling rate. This

Table 1
Thermal properties of samples A, B and C, measured from the DSC curves. ΔH_0 denotes the structural relaxation exothermic heat; ΔH_1 and ΔH_2 are the exothermic heats of the first and second crystallizations, respectively.

Sample	ΔH_0 (J/g)	ΔH_1 (J/g)	ΔH_2 (J/g)	$\sum \Delta H$ (J/g)
A	−4.2	−41.4	−3.3	−44.7
B	−3.9	−40.2	−3.1	−43.3
C	−2.4	−35.9	−2.5	−38.4

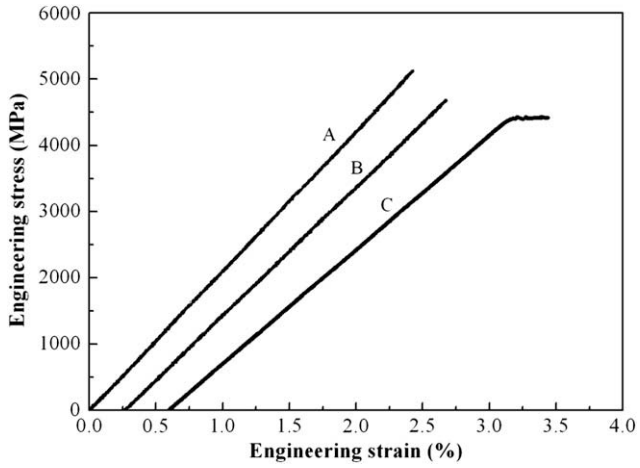

Fig. 4. Engineering stress–strain curves of samples A, B and C, subjected to the uniaxial compressive test at a constant strain rate of $1 \times 10^{-4}\ s^{-1}$.

indicates that the fragmentation degree is different. Besides the local cracks, a visible shear band was found on the outer surface of sample C. This indicates that shear deformation did occur, corresponding to the plasticity of 0.3%, although the sample displayed a brittle fracture during the compressive test (Fig. 4).

Fig. 6(a) shows the typical fracture micrographs of sample A after compressive test. It seems to be a clear core at the edge of each fracture surface, where the crack initiated. Then the crack propagated along uniform direction with a radial pattern, due to the intrinsic isotropic structure of metallic glass. Recently, it is found that one of the typical cleavage fracture features in brittle materials is dynamic instability induced by rapid crack propagation [21–24] with the ultimate velocity less than the Rayleigh wave velocity v_R [3,21,23]. Meanwhile, there is a visible smooth flat plane in the initial fracture region, like a mirror, with a large width about 170 μm, implying the free propagation of crack without any impediment. And then, the fracture surface becomes rougher with the micro-branching or bifurcation, corresponding to the so-called mist or hackle morphology. It implies that the dynamic crack velocity begins to exceed the critical velocity, v_C [25]. Fig. 6(b) shows plentiful cracks observed on the fracture surface. These cracks intersected with each other, and divided the surface into many parts, which formed many small fractured particles. In short, no vein-like patterns were observed on the fracture surfaces. Numerous cracks nucleated almost instantaneously at each fracture site, and then rapidly radiated with the dynamic instability just prior to the final fragmentation.

Fig. 7(a) shows the typical fracture morphology of sample B. The core, corresponding to the place of crack initiating, seems to be not clear. And then the crack propagated only along uniform direction with a slight radial pattern. Besides the visible ridges are perpendicular to the direction of the crack propagation [as indicated by arrows in Fig. 7(a)], there are no the mirror-like fracture surfaces. That suggests the crack propagation is along the curved face rather than the flat plane. This indicates that the crack propagation is disturbed with a slower speed, probably due to the intrinsic microstructure. Meanwhile, each curved face of crack propagation seems to become smaller, about 55 μm in width, only 1/3 of that of sample A. That illuminates the radiating range of the crack becomes smaller, suggesting the limited crack propagation. Between the curved faces, there are clear borderlines, along the direction of crack propagation. Furthermore, Fig. 7(b) shows a slightly melting liquid in a vein-like pattern observed at the corner of the ridge, indicating that the place has experienced a high temperature rise [26]. Meanwhile, the surface visibly becomes rough, comparing with that of sample A. Therefore, from the fracture morphologies above, it can be concluded that the crack propagation of sample B becomes slower, together with a little vein-like pattern.

Finally, Fig. 8(a) and (d) shows the typical fracture morphology of sample C. There are many straight lines, along the direction of crack propagation with a radiating pattern from the core, where the crack initiated [Fig. 8(a)]. That is the track of crack skimming over, named as "flow line". And, a visible shear band was found on the surface, intersecting with the flow lines at a constant angle. It is interesting to find that the "flow lines" were faulted seriously with a large distance, about 8.1 μm, indicating a high local plastic strain, which contributes to the macroscopic plasticity. Besides, many vein-like patterns appeared on the surface, erased by the friction during the fracture process [Fig. 8(b)], which is similar to that of the ductile metallic glass [23,27,28]. That implies a plastic strain at the local region, which is in agreement with the shear bands on the surface. Besides, some other melting liquid was erased into a flat plane, like the outspread milk, similar to the previous report [29]. The vein-like pattern can be attributed to the local melting within the main shear band, induced by the high elastic energy of the instantaneous fracture [30,31]. And under the effect of friction, the molten metallic glass easily flows and forms the vein-like pattern. Moreover, the amplified photo clearly shows that the melting liquid was wiped into a flat plane on the surface, and some vein-like patterns were presented in the gap of the cracks [Fig. 8(c)]. This implies that the melting behavior not only took place on the surface, but also appeared in the gap of the crack, which were resulted from the temperature rise inside the shear bands. Those observations provide a powerful evidence for the local shear strain. Furthermore, it is significant to find that there are some shear bands at the tip of the main crack along the crack propagation direction [Fig. 8(d)], suggesting a blunt behavior, similar to the report before [32]. That indicates a sound toughness with a high fracture toughness, K_C. In short, the sample C shows a certain plastic stain with the improved toughness, not only in the macroscopic compressive deformation, but also in the microscopic local fracture process.

Table 2
Compressive mechanical properties of samples A, B and C at a constant strain rate of $1 \times 10^{-4}\ s^{-1}$.

Sample	E (GPa ± 5)	σ_y (MPa ± 50)	σ_f (MPa ± 50)	ε_e (% ± 0.02)	ε_p (% ± 0.02)
A	214	–	5100	2.4	0
B	194	–	4700	2.4	0
C	175	4400	4400	2.6	0.3

4. Discussions

4.1. Microstructures

By comparing the results listed in Table 1, the sum of crystallization enthalpy, $\sum \Delta H$ decreases from 44.7 to 38.4 J/g. This trend should be mainly associated with the structural difference. First of all, it is certain that the microstructure is decided by cooling rate. The sample C, in the lowest cooling rate among the three samples, has been identified as a metallic glass composite with in situ precipitated dendritic crystalline phases. Because the cooling rate of sample B is between that of samples A and C, it should contain a large degree of short-range ordering and medium-range ordering, or even nanocrystals, although it has been identified as fully amorphous alloy by the XRD record. Besides, Table 3 shows that the extent of undercooled liquid region, ΔT_x, monotonically decreases, due to the increase in the degree of ordering for the three samples.

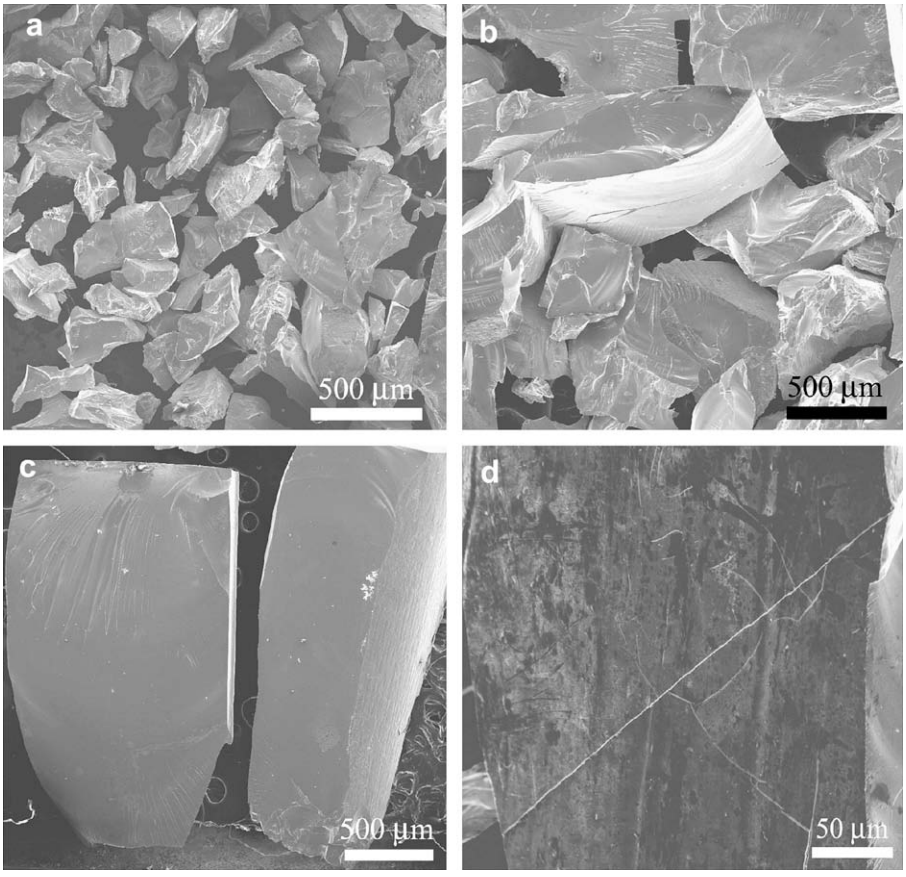

Fig. 5. SEM images of samples A, B and C, after compressive fracture: (a–c) fractured particles with different sizes for samples A, B and C, respectively; (d) shear band together with some cracks on the surface of sample C.

That furthermore offers the evidence that the sample B contains a larger degree of ordering than that of sample A.

In addition, as proposed by Cohen and Turnbull [33], during cooling of a glass-forming material from the liquid state or above the glass-transition temperature T_g, some excess quenched-in free volumes, as a structural defect, are trapped into the glassy state. The quantity of the excess free volume is, in fact, determined by the cooling rate. The lower cooling rate means that more atoms have enough time to move to their local ordered equilibrium positions. Thereby, a more ordered packing atomic structure forms during the cooling process from melting liquid. And, in turn, the obtained glassy sample possesses a smaller amount of free volume. As a result, the amount of free volume per atomic volume becomes smaller and smaller for samples A, B and C, due to the decrease in cooling rate. However, it is impossible to make quantitative statements about the amount of atomic-scale free volume in non-crystalline systems. But numerous attempts have been made to use DSC to characterize the change in free volume, relating closely to structural relaxation in amorphous alloys [34,35]. In the DSC thermogram, the exothermic reaction, seen just below the glass transition, is the result of the annihilation of free volume and structural relaxation. Slipenyuk and Eckert [35] noted that the change in free volume is proportional to the heat released during relaxation, i.e.,

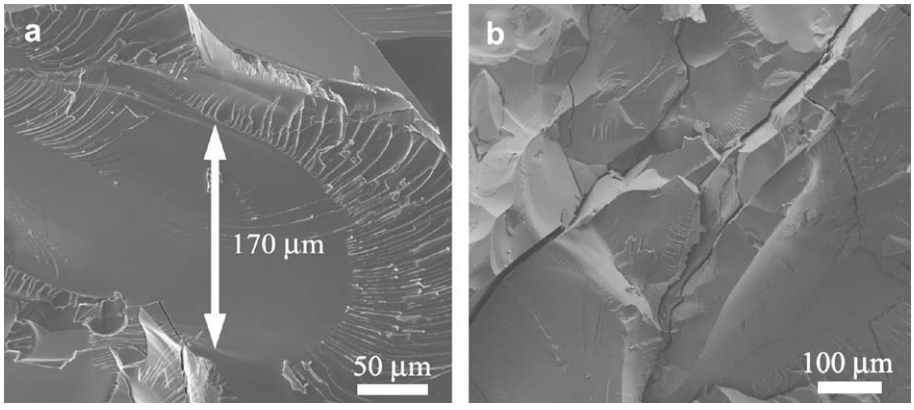

Fig. 6. SEM images of sample A after compressive fracture, (a) speedy crack propagation with a flat fracture surface; (b) many interacting cracks.

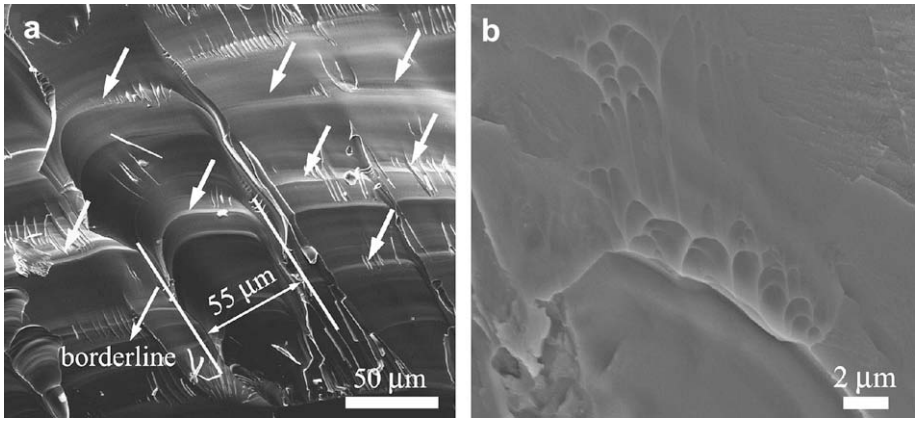

Fig. 7. SEM fractographies of sample B, after compressive fracture, (a) slower crack propagation with a curved fracture surface; (b) a few slightly melting droplets at the corner of the fracture ridge.

$$(\Delta H)_{\mathrm{fv}} = \beta' \Delta v_{\mathrm{f}} \quad (2)$$

where, β' is a constant; $(\Delta H)_{\mathrm{fv}}$ is the change in enthalpy; and Δv_{f} is the change in free volume per atomic volume. Therefore, a semi-quantitative difference in free volume for the three samples may be obtained. Here, we assume that in this work, the value of free volume per atomic volume for sample A is ψ_0. The ΔH_0, associating with the exothermic peak, was calculated by integrating the heat flow near the glass transition range (600–915 K). By substituting the values of ΔH_0 (Table 1 and inset in Fig. 3) into Eq. (3), the values of free volume per atomic volume for samples B and C are roughly estimated to be $0.93\psi_0$ and $0.57\psi_0$, respectively. That suggests the sample B contains less free volume per atomic volume than that of the sample A. And the sample C contains the least free volume per atomic volume together with some dendritic crystalline phases, due to the lowest cooling rate. Thus, the different microstructures must exert a strong influence on the mechanical properties of metallic glass. For the two fully amorphous samples A and B, it is known that the Young's modulus, E declines from 214 GPa to 194 GPa, and the strength declines from 5100 GPa to 4700 GPa, due to the change in the microstructure. However, for sample C, its Young's modulus, E and strength decline down to 175 GPa and 4400 GPa, respectively. But a plastic strain of about 0.3% happened, due to the in situ precipitated dendritic crystalline phases.

4.2. Fragmentation fracture

It is well known that there exists two stresses, i.e., shear stress and normal stress, on any shear plane of a metallic glass sample, subjected to a compressive load [4,8,36], as illustrated in Fig. 9(a). If the critical shear strength, τ_0, of the glassy sample is lower than the half of the compressive strength, σ_{C}, i.e., $\tau_0 < \sigma_{\mathrm{C}}/2$, the shear band

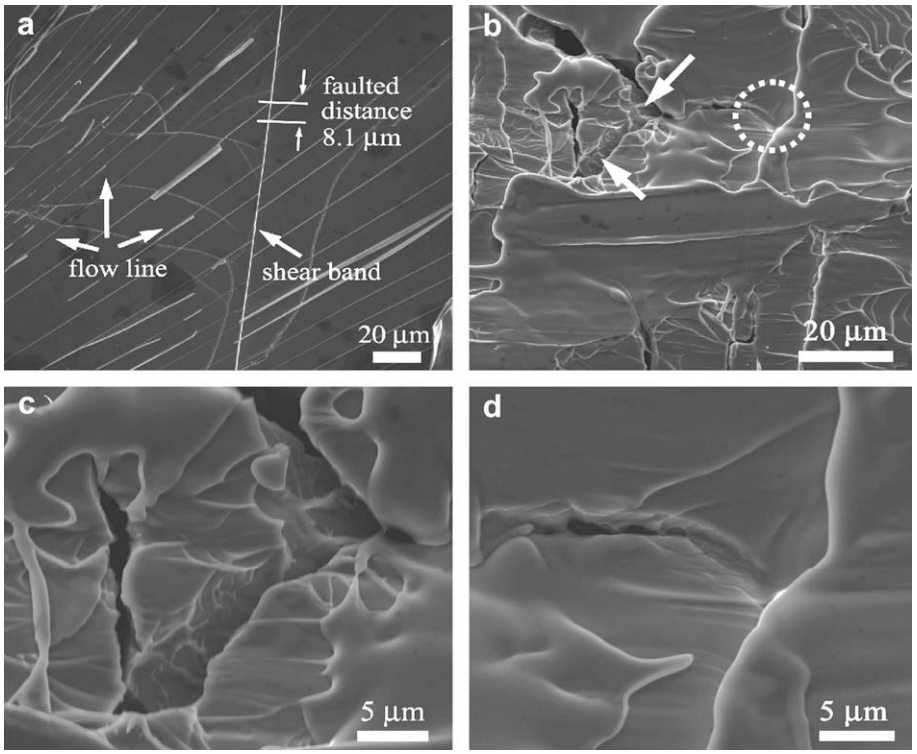

Fig. 8. SEM fractographies of sample C after compressive fracture, (a) faulted surface due to the shear deformation; (b) vein-like structure together with some cracks; (c) vein-like structure in the gap of crack, and (d) shear bands at the tip of the crack, suggesting a high fracture toughness.

Table 3
Thermal data of samples A, B and C, measured from the DSC curves, denoting T_g, T_{x1}, ΔT and T_{x2}.

Sample	T_g (K)	T_{x1} (K)	ΔT (K)	T_{x2} (K)
A	905	976	71	1175
B	917	977	60	1179
C	929	984	55	1176

will initiate and propagate approximately along the maximum shear stress plane, leading to the final shear failure. That can be widely observed in many Zr-, Cu-, and Ni-based BMGs under compression, displaying a sound plasticity [4,8,36–38]. On the other hand, it is often considered that the plasticity of metallic glass is associated with the free volume [39,40]. Therefore, the plastic deformation behavior is commonly interpreted in terms of flow defects, i.e., free volume [39,40]. Even a tiny change in the free volume could induce a dramatic effect on the plastic flow behavior of metallic glass [41,42]. Generally, the sites with a higher amount of free volume are expected to have lower strength, and are susceptive to the loading stress. So, these sites are considered as preexisting weakened regions with the kinetic equilibrium [43,44]. The differences in elastic properties between these regions and the surroundings may introduce stress concentrations during deformation, favoring the initial nucleation of shear bands [45].

However, if the critical shear strength, τ_0, is considerably higher than the half of the compressive strength, σ_C, i.e., $\tau_0 \geq \sigma_C/2$, it will be extremely difficult to stimulate the formation of shear band during compression. In this case, the metallic glass with high critical shear strength, τ_0, will have to fail in another mode rather than the shear fracture [4]. Previously, we have defined a parameter, $\alpha(\alpha = \tau_0/\sigma_0)$, as fracture mode factor. Where σ_0 is the critical cleavage fracture strength [8]. Therefore, the metallic glass in a fragmentation mode should have a relatively high fracture mode factor, $\alpha(\alpha = \tau_0/\sigma_0)$ [8]. During compression, according to the Hook's law, the uniaxial compressive stress, σ_C, and compressive elastic strain, ε_C, will follow the relation:

$$\sigma_C = E\varepsilon_C \tag{3}$$

where, E is the Young's modulus. When the metallic glass sample produces a compressive elastic strain, ε_C, there must yield a lateral tensile elastic strain, ε_T, due to Poisson's effect. Here, the two elastic strains, ε_T and ε_C satisfy the rule:

$$\nu = -\varepsilon_T/\varepsilon_C \tag{4}$$

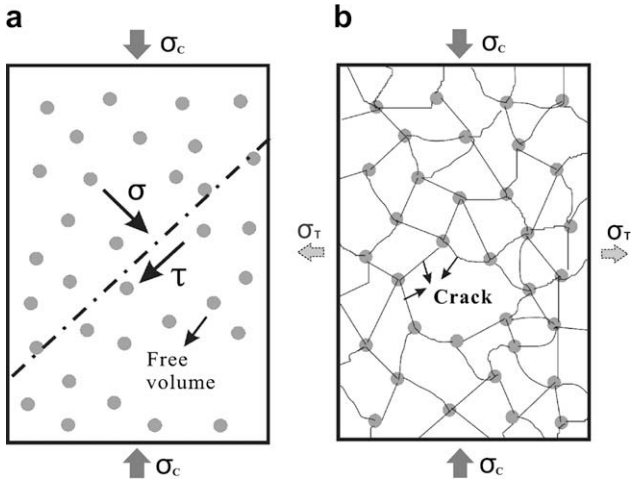

Fig. 9. Illustration of the fracture processes of Co-based metallic glass under the compressive test: (a) distribution of shear stress on the shear plane; (b) fragmentation processes due to the lateral tensile stress and plentiful simultaneously propagating cracks.

Where ν is Poisson's ratio. With the increase in the lateral tensile elastic strain, up to ε_T, a lateral tensile stress σ_T will apply to the metallic glassy sample, i.e.,

$$\sigma_T = E\varepsilon_T = \nu\sigma_C \tag{5}$$

This indicates that the lateral tensile stress σ_T is proportional to the compressive stress, σ_C. When σ_T is higher than the critical cleavage strength, σ_0 of the metallic glass, i.e., $\sigma_T > \sigma_0$, multiple cleavage fracture will inevitably occur [Fig. 9(b)], resulting in a fragmentation fracture feature [Fig. 5(a) and (c)]. From Eqs. (4–6), the following relations can be deduced:

$$\sigma_0 \leq \sigma_T = \nu\sigma_C \tag{6}$$

And

$$\tau_0 \geq \sigma_C/2 \tag{7}$$

Therefore, from Eqs. (7) and (8), it is easy to calculate the fracture mode factor as:

$$\alpha = \tau_0/\sigma_0 \geq 1/2\nu \tag{8}$$

Assuming that Poisson's ratio of the metallic glass is about 1/3, the fracture mode factor should be higher than 1.5, i.e., $\alpha = \tau_0/\sigma_0 \geq 1.5$. Just because of the high fracture mode factor [8], several kinds of metallic glasses, for example, Mg-, Co-, and Fe-based BMGs, often fail either in a fragmentation mode or in a distensile fracture mode under compressive loading [4,11,46–48].

Since Co-based metallic glass always exhibits extremely high shear resistance, it is always too late to induce the formation of shear bands before catastrophic failure. And the multiple cracks could be formed, due to the brittle character with a high fracture mode factor, $\alpha(\alpha = \tau_0/\sigma_0)$. Because the sites with a higher amount of free volume are considered as preexisting weakened regions with lower strength, the cracks might favor the initial nucleation at these sites, due to the stress concentrations introduced by the differences in elastic properties between these regions and the surroundings. That should correspond to the fracture sites, i.e., the core of crack radiation [Fig. 6(a)]. Because numerous of free volumes distribute homogeneously inside the metallic glass, many cracks nearly synchronously nucleate and propagate. And then they interact with each other, leading to the final fragmentation fracture, as illustrated in Fig. 9(b). Furthermore, for the samples A, B and C, due to the decrease in the free volume per atomic volume caused by the decrease in cooling rate, the number of fracture sites, i.e., the places of crack initiating, will become less and less. So, the number of cracks will become smaller, leading to the decrease in the fragmentation coefficient, F_n [11]. Besides, because the sample C contains the least free volume, its fracture sites should be the least. During the deformation, when the stress is up to high enough, the plastic deformation is first to be triggered in crystalline phase. And then, the cracks will initiate in the metallic glass matrix, due to its low plasticity. The relative report can be found in Ref. [48]. So the little free volume and in situ crystalline phases, caused by the decrease in cooling rate, contribute to the plastic deformation of sample C.

4.3. Melting induced by fracture

For the current investigated three samples, due to the intrinsic brittleness, the sample always fails in a fragmentation mode after the uniaxial compressive test. However, the fragmentation degree is always different, as shown in Fig. 5(a) and (c). To describe the fragmentation degree of the metallic glass, a concept of fragmentation coefficient, F_n was proposed in the following form [11],

$$F_n = A_n/A_0 \quad (9)$$

where, A_n is the area of new surface after fracture, and A_0 is the area of original surface before fracture. Due to the same geometry of samples A, B and C, the area of original surface, A_0 is the same. But the fractured particle sizes of samples A, B, and C increase one by one. So the area of new surface, A_n decreases correspondingly, which causes the decrease in the fragmentation coefficient, F_n, according to the definition above. Besides, it is well known that BMGs can store high elastic strain energy than conventional crystalline metallic materials during compression [30]. The elastic energy density, δ_E, stored in a metallic glass sample upon failure can be expressed as:

$$\delta_E = \frac{\sigma_f^2}{2E} \quad (10)$$

where, E is Young's modulus, and σ_f is the fracture strength of the BMG material. For the current samples A, B and C, the elastic energy density, δ_E is approximately equal. After fragmentation of the three samples, it assumes that η is the efficiency of the effective energy to be received by the new surface from elastic energy, and γ is the receiving energy of unit new surface, transformed from the elastic energy, causing the temperature rise. Thus, it can be expressed as:

$$\gamma = \frac{\eta\delta_E V_0}{A_n} = \frac{1}{F_n}\frac{\eta\delta_E V_0}{A_0} \quad (11)$$

where, V_0 is the original volume of the sample. So for the sample B, due to its smaller fragmentation coefficient, F_n, the receiving energy of unit new surface is greater than that of sample A. Thus, when the temperature rise, caused by the receiving energy, will be up to the melting point of material, the melting behavior is easy to happen. For sample C, due to the smallest fragmentation coefficient, F_n, from Eq. (11), it is easy to understand that much melting droplet was observed on the fracture surface. That contributes to the local plastic strain and blocks the crack propagation, so as to result in the formation of local shear bands. At the same time, due to the retarding effect of the melting liquid on the crack propagation, some shear bands were also observed at the tip of crack [Fig. 8(d)], suggesting an increase in the plastic zone size, r_p. Xi et al. [6] have demonstrated a correlation between plastic zone size, r_p, the fracture toughness K_C and yield strength σ_y as:

$$r_p = \frac{1}{6\pi}\left(\frac{K_C}{\sigma_y}\right)^2 \quad (12)$$

So it is easy to find that the fracture toughness, K_C, is proportional to $\sqrt{r_p}$, i.e., $K_C \propto \sqrt{r_p}$. This indicates a significant increase in the fracture toughness, K_C, due to the retarding effect of the melting liquid on the rapid crack propagation.

5. Conclusions

Co-based metallic glass and composite with dendrites were cast at the different cooling rates. Due to the decrease in cooling rate, the degree of order will become higher and higher. And even some dendritic crystalline phases were in situ precipitated from the metallic glass matrix. Besides, due to the decrease in cooling rate, the free volume becomes smaller, leading to the decrease in fracture site. Furthermore, that results in the decease in fragmentation coefficient, F_n after compressive fracture. Thus, the receiving energy of unit new surface from the elastic energy, γ, will enhance, which contributes to the local melting behavior. In addition, for sample C, the BMG composite, due to the associated contribution of the less free volume and in situ crystalline phases, the slight plasticity happened. And the local melting liquid made a retarding effect on the crack propagation, leading to the enhanced plastic zone, r_p and fracture toughness, K_C. Based on these findings, it is suggested that cooling rate is a critical factor to control the microstructure and mechanical properties of Co-based metallic glass, which has an instructional significance for the optimizing design of the high-performance materials.

Acknowledgements

The authors would like to acknowledge Q.Q. Duan, P. Zhang and H. F. Zou for the mechanical testing and SEM observations. This work was financially supported by the National Outstanding Young Scientist Foundation under Grant Nos. 50625103 and 50825103, the National Natural Science Foundation of China (NSFC) under Grant Nos. 50871117 and 50890173 and the "Hundred of Talents Project" by Chinese Academy of Sciences.

References

[1] Klement W, Willens RH, Duwez P. Nature 1960;187:869.
[2] Schuh CA, Hufnagel TC, Ramamurty U. Acta Mater 2007;55:4067.
[3] Johnson WL. MRS Bull 1999;24:42.
[4] Zhang ZF, Wu FF, He G, Eckert J. J Mater Sci Technol 2007;23:747.
[5] Lewandowski JJ, Wang WH, Greer AL. Philos Mag Lett 2005;85:77.
[6] Xi XK, Zhao DQ, Pan MX, Wang WH, Wu Y, Lewandowski JJ. Phys Rev Lett 2005;94:125510.
[7] Mattoni A, Colombo, Cleri LF. Phys Rev Lett 2005;95:115501.
[8] Zhang ZF, Eckert J. Phys Rev Lett 2005;94:094301.
[9] Wu WF, Li Y, Schuh CA. Philos Mag 2008;88:71.
[10] Menzel BC, Dauskardt RH. Acta Mater 2008;56:2955.
[11] Zhang ZF, Zhang H, Shen BL, Inoue A, Eckert J. Philos Mag Lett 2006;86:643.
[12] Wang WH, Dong C, Shek CH. Mater Sci Eng R 2004;44:45.
[13] Das J, Tang MB, Kim KB, Theissmann R, Baier F, Wang WH, et al. Phys Rev Lett 2005;94:205501.
[14] Hays CC, Kim CP, Johnson WL. Phys Rev Lett 2000;84:2901.
[15] Guo FQ, Wang HJ, Poon SJ, Shiflet GJ. Appl Phys Lett 2005;86:091907.
[16] Fan JT, Zhang ZF, Jiang F, Sun J, Mao SX. Mater Sci Eng A 2008;487:144.
[17] Huang YJ, Shen J, Sun JF. Appl Phys Lett 2007;90:081919.
[18] Imafuku M, Sato S, Nakamura T, Koshiba H, Matsubara E, Inoue A. Mater Res Soc Symp Proc 2001;644:L161.
[19] Bian Z, Kato H, Qin CL. Acta Mater 2005;53:2037.
[20] Gilbert CJ, Ager JW, Schroeder V, Ritchie RO, Lloyd JP, Graham JR. Appl Phys Lett 1999;74:3809.
[21] Lin XH, Johnson WL. J Appl Phys 1995;78:6514.
[22] Oh JC, Ohkubo T, Kim YC, Fleury E, Hono K. Scripta Mater 2005;53:165.
[23] Leonhard A, Xing LQ, Heilmaier M, Gebert A, Eckert J, Schultz L. Nanostruct Mater 1998;10:805.
[24] Zhang ZF, Wu FF, Gao W, Tan J, Wang ZG, Stoica M, et al. Appl Phys Lett 2006;89:251917.
[25] Johnson JW, Holloway DG. Philos Mag 1966;14:731.
[26] Lewandowski JJ, Greer AL. Nat Mater 2006;5:15.
[27] Fan JT, Wu FF, Zhang ZF, Jiang F, Sun J, Mao SX. J Non-cryst Solids 2007;353:4707.
[28] Subhash G, Dowding RJ, Kecskes LJ. Mater Sci Eng A 2002;334:33.
[29] Fan JT, Zhang ZF, Shen BL, Mao SX. Scripta Mater 2008;59:603.
[30] Wright WJ, Saha R, Nix WD. Mater Trans 2001;42:642.
[31] Liu CT, Heatherly L, Easton DS, Carmichael CA, Schneibel JH, Chen CH. Metall Mater Trans A 1998;29:1811.
[32] Flores KM, Dauskardt RH. Scripta Mater 1999;41:937.
[33] Turnbull D, Cohen MH. J Chem Phys 1970;52:3038.
[34] Bhowmick R, Raghavan R, Chattopadhyay K, Ramamurty U. Acta Mater 2006;54:4221.
[35] Slipenyuk A, Eckert J. Scripta Mater 2004;50:39.
[36] Zhang ZF, Eckert J, Schultz L. Acta Mater 2003;51:1167.
[37] Nieh TG, Wadsworth J, Liu CT, Ohkubo T, Hirotsu Y. Acta Mater 2001;49:2887.
[38] Shen J, Huang YJ, Sun JF. J Mater Res 2007;22:3067.
[39] Yang B, Liu CT, Nieh TG. Appl Phys Lett 2006;88:221911.
[40] Argon AS. Acta Metall 1979;27:47.
[41] Murah P, Ramamurty U. Acta Mater 2005;53:1467.
[42] Hey PD, Sietsma J, Van Den Beukel A. Acta Mater 1998;46:5873.
[43] Tuinster P, Duine PA, Sietsma J, Vandenbeukel A. Acta Metall Mater 1995;43:2815.
[44] Steif PS, Spaepen F, Hutchinson JW. Acta Metall 1982;30:447.
[45] Kanungo BP, Glade SC, Asoka-Kumar P, Flores KM. Intermetallics 2004;12:1073.
[46] Stoica A, Eckert J, Roth S, Zhang ZF, Schultz L, Wang WH. Intermetallics 2005;13:764.
[47] Shen BL, Chang CT, Zhang ZF, Inoue A. J Appl Phys 2007;102:023515.
[48] Zhang H, Pan XF, Zhang ZF, Das J, Kim KB, Muller C. Z Metallkd 2005;96:675.